Computational Materials Science 233 (2024) 112722

Contents lists available at ScienceDirect

Computational Materials Science

journal homepage: www.elsevier.com/locate/commatsci

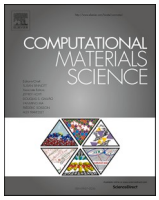

Full Length Article

Interatomic potentials for cubic zirconia and yttria-stabilized zirconia optimized by genetic algorithm

Susumu Fujii [a,b,*], Akihide Kuwabara [b,c]

[a] Division of Materials and Manufacturing Science, Osaka University, Suita, Osaka 565-0871, Japan
[b] Nanostructures Research Laboratory, Japan Fine Ceramics Center, Atsuta, Nagoya 456-8587, Japan
[c] Next Generation Zirconia Social Cooperation Program, Institute of Engineering Innovation, The University of Tokyo, Bunkyo-ku, Tokyo, Japan

ARTICLE INFO

Keywords:
Zirconia
Yttria-stabilized zirconia
Interatomic potential
Molecular dynamics
Ab initio calculation
Genetic algorithm

ABSTRACT

Yttria stabilized zirconia (YSZ) is an important engineering ceramic oxide used for various applications, including solid electrolytes in solid oxide fuel cells due to its high ionic conductivity. Accurate and computationally inexpensive interatomic potentials for cubic ZrO_2 and YSZ are required to accommodate the large number of defect configurations originating from high concentrations of Y and oxygen vacancies and to statistically understand their properties in realistic time. In this study, a genetic algorithm has been used to optimize empirical interatomic potential parameters for cubic ZrO_2 and $10Y_2O_3$ mol% YSZ using energies, forces acting on atoms, and stresses generated by *ab initio* calculations as training data. The optimized potentials reproduce the structural, mechanical, and thermal properties as well as the ionic conduction properties more accurately than previously reported empirical interatomic potentials. The developed potentials will be useful for a statistical characterization of YSZ properties, combined with more accurate *ab initio* calculations.

1. Introduction

Zirconia, represented by the chemical formula of ZrO_2, is one of the most studied ceramic oxides because of its broad range of technological applications [1–6]. ZrO_2 forms a monoclinic crystal structure at room temperature and undergoes phase transitions to tetragonal and cubic phases at high temperatures [7,8]. The cubic fluorite structure (Fig. 1a) can be stabilized by doping cations of larger size than zirconium ions [8–10]. An important dopant is yttria Y_2O_3, where high concentrations of Y^{3+} not only stabilize the cubic structure but also create a large number of oxide-ion vacancies, allowing oxide-ion conduction in ZrO_2 system. Y_2O_3-doped ZrO_2, so-called yttria-stabilized zirconia (YSZ) (Fig. 1b), is one of the most important oxide-ion conductors and is widely used as solid electrolytes in solid oxide fuel cells (SOFCs) and oxygen sensors [1,2,11–15].

Because of the importance of YSZ for technological applications and as a model material, theoretical calculations on its defect configurations and properties have been extensively performed over the past four decades [13,16–25]. The calculations for YSZ are computationally expensive because (1) YSZ involves high concentrations of point defects with a large number of possible defect configurations, requiring large supercells containing many ions; (2) analyses of ion dynamics, such as oxide-ion diffusion, requires long-time molecular dynamics (MD) simulations. Thus, several empirical interatomic potentials (EIPs), including the Coulomb-Buckingham potentials, have been constructed [13,17,26], which are much less computationally expensive than *ab initio* calculations. The use of these potentials has revealed the nature of YSZ, such as the mechanisms of ionic conduction [13,16,20,27,28] and grain boundary segregation of Y and Vo [21–23].

Although *ab initio* calculations have been confirmed to be consistent with experiments in many fields, the accuracy of EIPs is controversial. In recent years, machine learning potentials (MLPs) have been developed for ZrO_2 and YSZ, which reproduce the structure, energy, and force of ZrO_2-Y_2O_3 system with high accuracy approaching that of *ab initio* calculations [29–34]. The computational cost of MLPs is several orders of magnitude lower than that of *ab initio* calculations, allowing more accurate simulations with moderate scales. However, they are still several orders of magnitude more expensive than EIPs [35,36] and are often too time-consuming for large-scale calculations. A combined use of *ab initio* calculations, MLPs, and EIPs, depending on the required accuracy and computational cost, is necessary to elucidate the nature of YSZ. In this regard, it is important to improve the accuracy of EIPs, especially for the comprehensive analyses of defect configurations and ion dynamics.

EIPs constructed over a few decades were based on parameter fitting

* Corresponding author at: Division of Materials and Manufacturing Science, Osaka University, Suita, Osaka 565-0871, Japan.
E-mail address: susumu.fujii@mat.eng.osaka-u.ac.jp (S. Fujii).

https://doi.org/10.1016/j.commatsci.2023.112722
Received 6 July 2023; Received in revised form 2 November 2023; Accepted 4 December 2023
Available online 14 December 2023

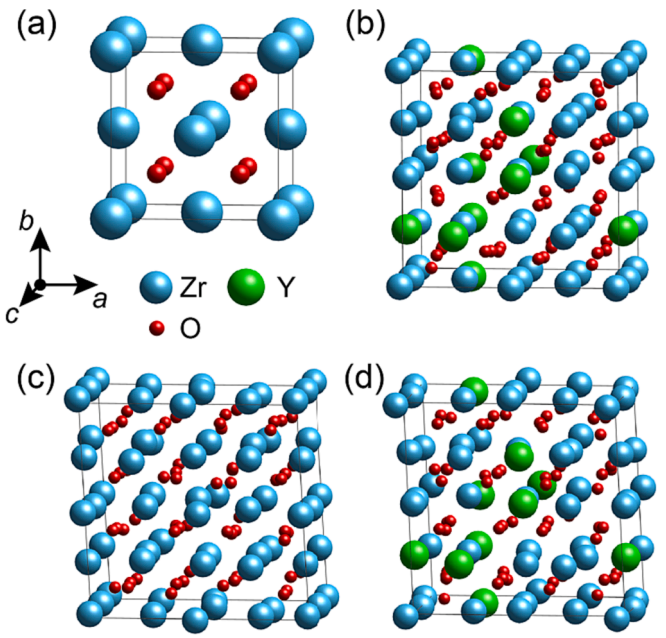

Fig. 1. (a) Crystal structure of cubic fluorite ZrO_2. (b) 10YSZ model with the lowest energy among the training and test datasets. (c) An example of deformed ZrO_2 models. (d) An example of deformed 10YSZ models.

to reproduce the structure and specific material properties of ZrO_2 and YSZ. Recently, alternative methods have been proposed that utilize machine learning techniques to efficiently create more accurate EIPs [37–39]. For example, Rohskopf *et al.* demonstrated that phonons and thermal conductivity of silicon and germanium can be accurately reproduced by EIPs optimized using a genetic algorithm and *ab initio* datasets [37]. Applying such a machine learning approach to cubic ZrO_2 and YSZ may produce more accurate EIPs.

Here, we report a genetic algorithm optimized potential (GAOP) for cubic ZrO_2 and 10 mol% Y_2O_3 YSZ (10YSZ), trained on a large dataset generated by *ab initio* calculations. By efficiently exploring a vast number of potential parameter combinations via a genetic algorithm, the developed GAOP exhibits energies, forces, and stresses closer to *ab initio* calculations than previously reported EIPs. To evaluate the performance of the GAOP, structural, mechanical, thermal, and ionic conduction properties are calculated and compared with experiments and *ab initio* calculations. With its low computational cost and improved accuracy, the GAOP is useful for large-scale calculations that are practically difficult to perform using MLP-based and *ab initio* calculations (*e.g.*, oxide-ion conduction in large cells), and for pre-screening stable defect configurations in YSZ (*e.g.*, Monte Carlo search for Y segregation at grain boundaries) prior to more accurate MLP-based and *ab initio* calculations.

2. Methods

2.1. Datasets

The energies, forces acting on atoms, and stresses in cubic ZrO_2 and 10YSZ were obtained from *ab initio* calculations as training and test datasets for EIPs, as also used in ref. [40]. We created a 2 × 2 × 2 supercell of the conventional unit cell of cubic ZrO_2, which contains 96 atoms. 10YSZ models were constructed by randomly replacing 6 Zr atoms with Y atoms and introducing 3 oxygen vacancies V_O in the cubic ZrO_2 supercell (Fig. 1b). Twenty and two 10YSZ models with different Y and V_O configurations were constructed for the training and test datasets, respectively. The lattice parameters and atomic positions of the cubic ZrO_2 and 10YSZ models were optimized until the atomic residual forces were less than 1.0×10^{-2} eVÅ^{-1}. The lattice parameter a of these supercells is approximately 10 Å.

Following Seko *et al.* [41], we introduced structural deformations, *i.e.*, random lattice distortion and atomic displacements, into each cubic ZrO_2 and 10 YSZ model:

$$\boldsymbol{A}' = \boldsymbol{A} + \varepsilon_A \boldsymbol{R}, \tag{1}$$

$$\boldsymbol{f}' = \boldsymbol{f} + \varepsilon_f \boldsymbol{A}'^{-1} \boldsymbol{\eta}, \tag{2}$$

where $\boldsymbol{A}$ and $\boldsymbol{A}'$ are the lattice vectors of the supercell, and $\boldsymbol{f}$ and $\boldsymbol{f}'$ are the fractional coordinates of the atoms in the supercell. $\boldsymbol{R}$ and $\boldsymbol{\eta}$ are a (3 × 3) matrix and a three-dimensional vector, respectively, containing random numbers between −1 and 1 to introduce random lattice distortion and atomic displacements. ε_A and ε_f are parameters to control the magnitude of the lattice distortion and atomic displacements. For

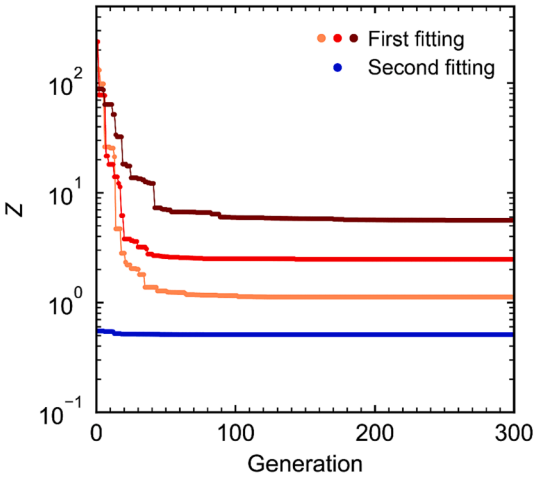

Fig. 2. Examples of Z convergence with generations in the first and second genetic algorithm optimization.

Table 1
Parameter ranges of the Coulomb-Buckingham potential considered in the genetic algorithm and their optimal values for cubic ZrO_2 and 10YSZ. The values of potential parameters reported by Grimes et al. [26] and Kilo et al. [13] are also shown. See also Fig. S2 for the plots of energy vs. interatomic distance.

	Parameter	Range	GAOP	Grimes	Kilo
Charge	q (e)	0.00–1.00	0.55	1.0	1.0
Zr-O	A (eV)	100.00–50000.00	6434.96	1502.11	1024.6
	ρ (Å)	0.0100–1.0000	0.2304	0.3477	0.376
	C (eVÅ^6)	1.000–500.000	8.674	5.1	0.0
O-O	A (eV)	100.00–50000.00	11994.52	9547.96	22764
	ρ (Å)	0.0100–1.0000	0.2219	0.2192	0.149
	C (eVÅ^6)	1.000–500.000	2.949	32.0	27.89
Y-O	A (eV)	100.00–50000.00	12575.00	1766.40	1325.6
	ρ (Å)	0.0100–1.0000	0.2324	0.33849	0.3461
	C (eVÅ^6)	1.000–500.000	68.491	19.43	0.0

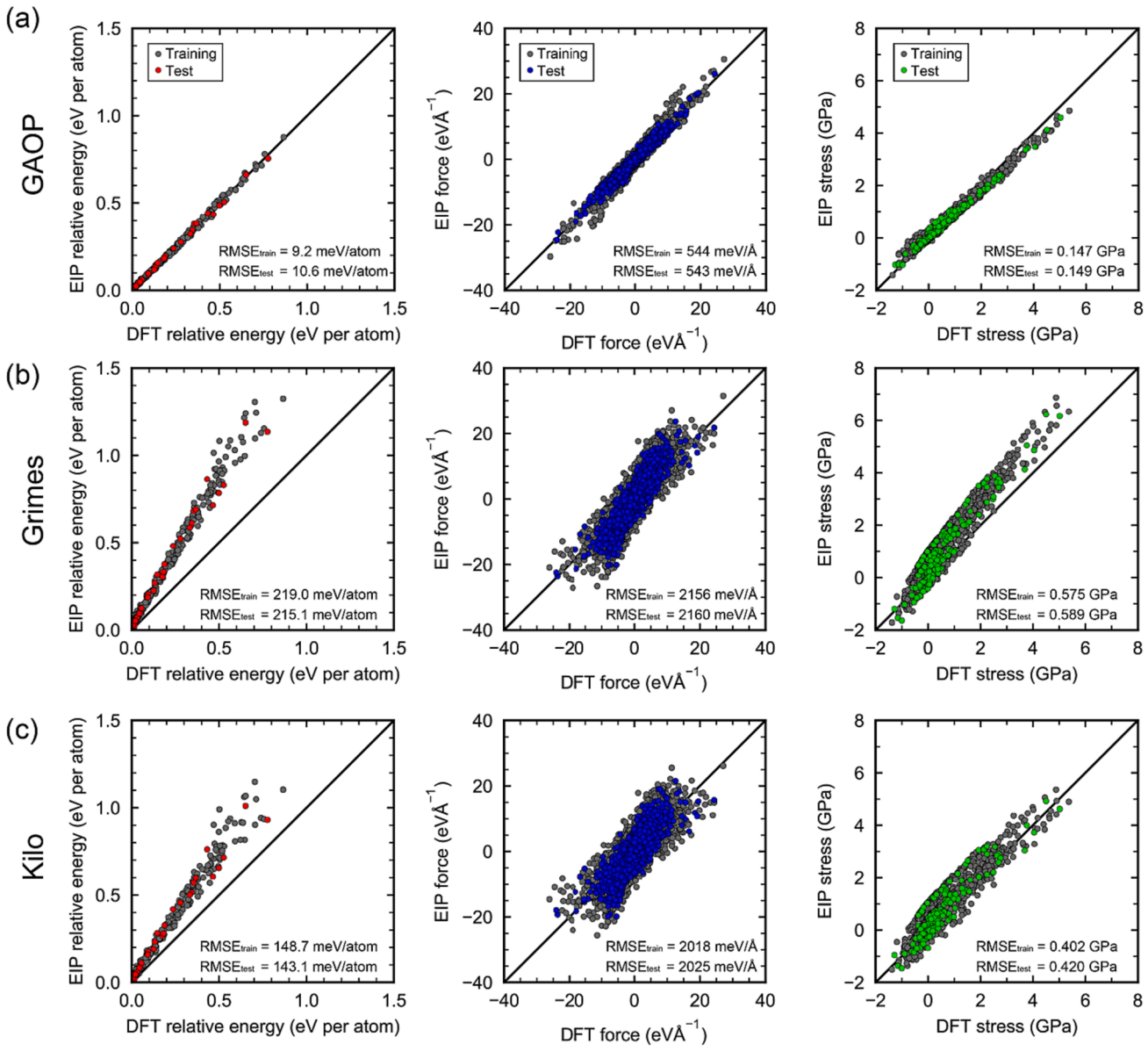

Fig. 3. Comparison of energies, forces, and stresses calculated using the EIPs and DFT. (a) The developed GAOP. (b) The potential reported by Grimes et al. [26] (c) The potential reported by Kilo et al. [13] The values calculated from the models used for the GAOP training and testing are plotted with gray and colored points, respectively. The diagonal line indicates that the values calculated by EIP and DFT are equal. The root mean squared errors (RMSEs) are also indicated in the panels.

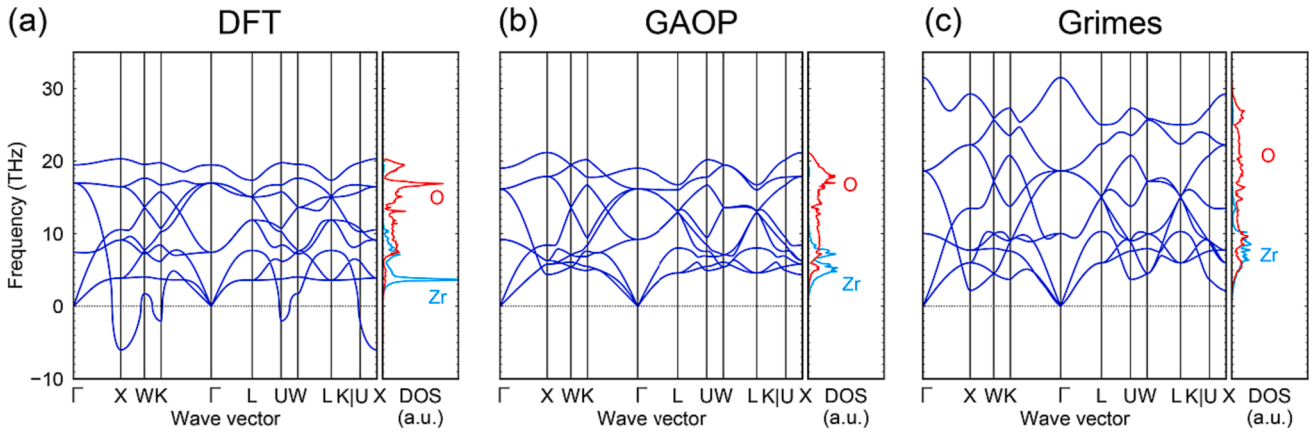

Fig. 4. Phonon band structures and partial density of states of Zr and O obtained by (a) DFT calculations, (b) the GAOP, and (c) the potential reported by Grimes et al. [26].

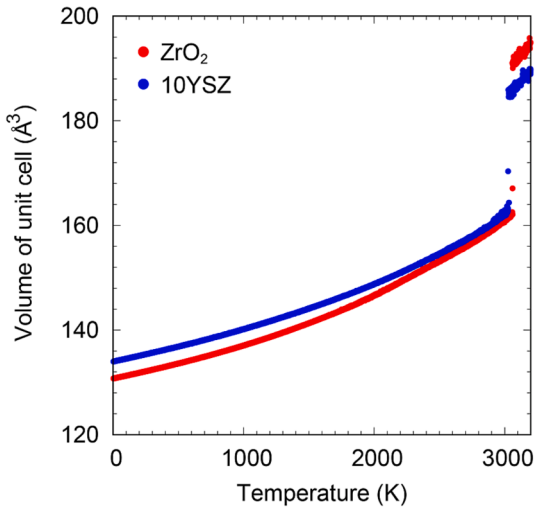

Fig. 5. Volume of ZrO_2 and YSZ models normalized to the size of the unit cell as a function of temperature. The GAOP was used for the calculation.

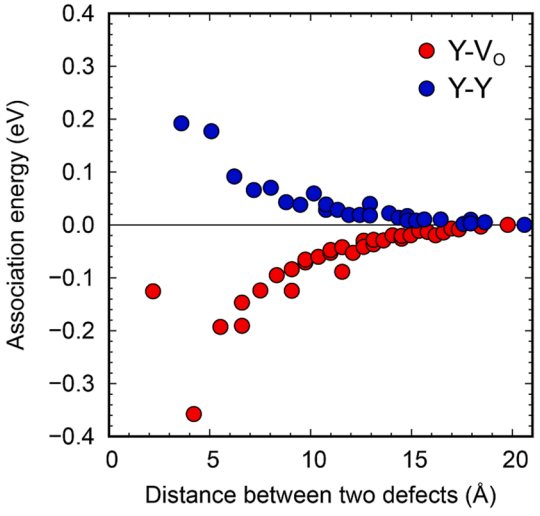

Fig. 6. Association energies of Y'_{Zr}-$V_O^{\bullet\bullet}$ and Y'_{Zr}-Y'_{Zr} pairs as a function of their distance. The GAOP was used for the calculation.

cubic ZrO_2, 100 deformations were generated for training and 10 for testing. For 10YSZ, 10 deformations were generated for each model. The values of ε_A and ε_f for the Nth distortion and displacements were set to $\varepsilon_A = 0.50\ N/N_{\text{total}}$ Å and $\varepsilon_f = 0.25\ N/N_{\text{total}}$ Å to include various deformations. The examples of the deformed models are shown in Fig. 1c and d. The energies, forces, and stresses calculated from these deformed models were used as the training and test datasets.

Structure optimization of the supercells and evaluations of the energies, forces, and stresses of the deformed models were performed using density functional theory (DFT) calculations with the plane-wave basis projector augmented wave (PAW) method [42] implemented in the Vienna *Ab initio* Simulation Package (VASP) [43,44]. The generalized gradient approximation (GGA) in the form of PBEsol [45] was employed. The plane-wave energy cutoff was set to 500 eV. The Brillouin zone was sampled with a Monkhorst-Pack k-point grid of $2 \times 2 \times 2$ [46]. The valence configurations of the PAW potentials used in this study were follows: [$4s^2\ 4p^6\ 5s^2\ 4d^2$] for Zr, [$4s^2\ 4p^6\ 5s^2\ 4d^1$] for Y, and [$2s^2\ 2p^4$] for O. The rest electrons were treated as fixed core electrons. The total energy convergence was set to 1.0×10^{-6} eV/cell. See Fig. S1 for the convergence of DFT results and the effect of Hubbard U correction.

2.2. Potential optimization by genetic algorithm

We optimized Buckingham interatomic potential parameters of Zr-O, O-O, and Y-O for short-range interactions and effective atomic charges of Zr, O, and Y for long-range Coulombic interactions, using a genetic algorithm with the datasets generated by *ab initio* calculations. The Coulomb-Buckingham potential is widely used to describe the nature of Coulombic systems and is defined as follows [47]:

$$\Phi_{ij}(r_{ij}) = A\exp\left(-\frac{r_{ij}}{\rho}\right) - \frac{C}{r_{ij}^6} + \frac{q_i q_j}{4\pi\varepsilon_0 r_{ij}}, \tag{3}$$

where Φ_{ij} and r_{ij} are the potential energy and distance of atoms i and j, A, ρ, and C are the parameters of the Buckingham potential, and q_i and q_j are the charges of atoms i and j, and ε_0 is the vacuum permittivity. The cutoff distance was set to 12.0 Å in this study. The parameter ranges considered in the genetic algorithm optimizations are listed in Table 1.

First, the potential parameters of Zr-O and O-O as well as the effective atomic charges of Zr, Y, and O were fitted by a genetic algorithm, followed by fitting the parameters of Y-O. To maintain the charge neutrality of the system, the effective charges of Zr, O, and Y should be defined as $4q$, $-2q$, and $3q$ to reflect their formal charges, with q being the only parameter used to determine the effective charges. The first training dataset for Zr and O contains one optimized and 100 deformed cubic ZrO_2 models. The total number of energies, forces, and stresses for training were 101, 29088, and 606, respectively, against seven variable parameters to be fitted. On the other hand, the second training dataset for the Y-O interaction contains one optimized 10YSZ model with the lowest energy (Fig. 1b) and 200 deformed 10YSZ models. The total number of energies, forces, and stresses for training were 201, 56079, and 1206, respectively, against three variable parameters to be fitted.

As a genetic algorithm approach, the code POPs [37], developed by Rohskopf *et al.* for the optimization of interatomic potentials, was used. The procedure of the genetic algorithm is as follows [37]: (1) create a population of N_p individuals with random genotypes (describing potential parameters in this case); (2) evaluate the fitness of the individuals by the objective function Z; (3) include the superior individuals with low Z in the next generation (elite); (4) combine the genotypes of two individuals (parents) to create a new genotype in the next generation (offspring); (5) change the genotype of the offspring randomly (mutation); (6) repeat the steps of (2)-(5) N_g times. N_p and N_g were set to 1000 and 300, respectively. The elite and mutation percentages were set at 5 % and 40 %, respectively. The high percentage of mutation is to prevent the potential parameters from falling into local minima. The fitting by the genetic algorithm was performed 100 times for the first fitting and 30 times for the second fitting with different initial populations with random genotypes.

The objective function Z is defined in the literature [37] as follows:

$$Z = w_e Z_e + w_f Z_f + w_s Z_s, \tag{4}$$

where Z_e, Z_f and Z_s are the errors of energy, force, and stress, and w_e, w_f and w_s are the weights of Z_e, Z_f and Z_s. The errors of energy, force, and stress are defined as follows:

$$Z_e = \frac{\sum_j^M \left(E_j^{\text{DFT}} - E_j^{\text{EIP}}\right)^2}{M\sum_j^M \left(E_j^{\text{DFT}}\right)^2} \tag{5}$$

$$Z_f = \frac{\sum_j^M \sum_i^{N_j} \|\boldsymbol{F}_{ij}^{\text{DFT}} - \boldsymbol{F}_{ij}^{\text{EIP}}\|^2}{\sum_j^M N_j \sum_j^M \|\boldsymbol{F}_{ij}^{\text{DFT}}\|^2}, \tag{6}$$

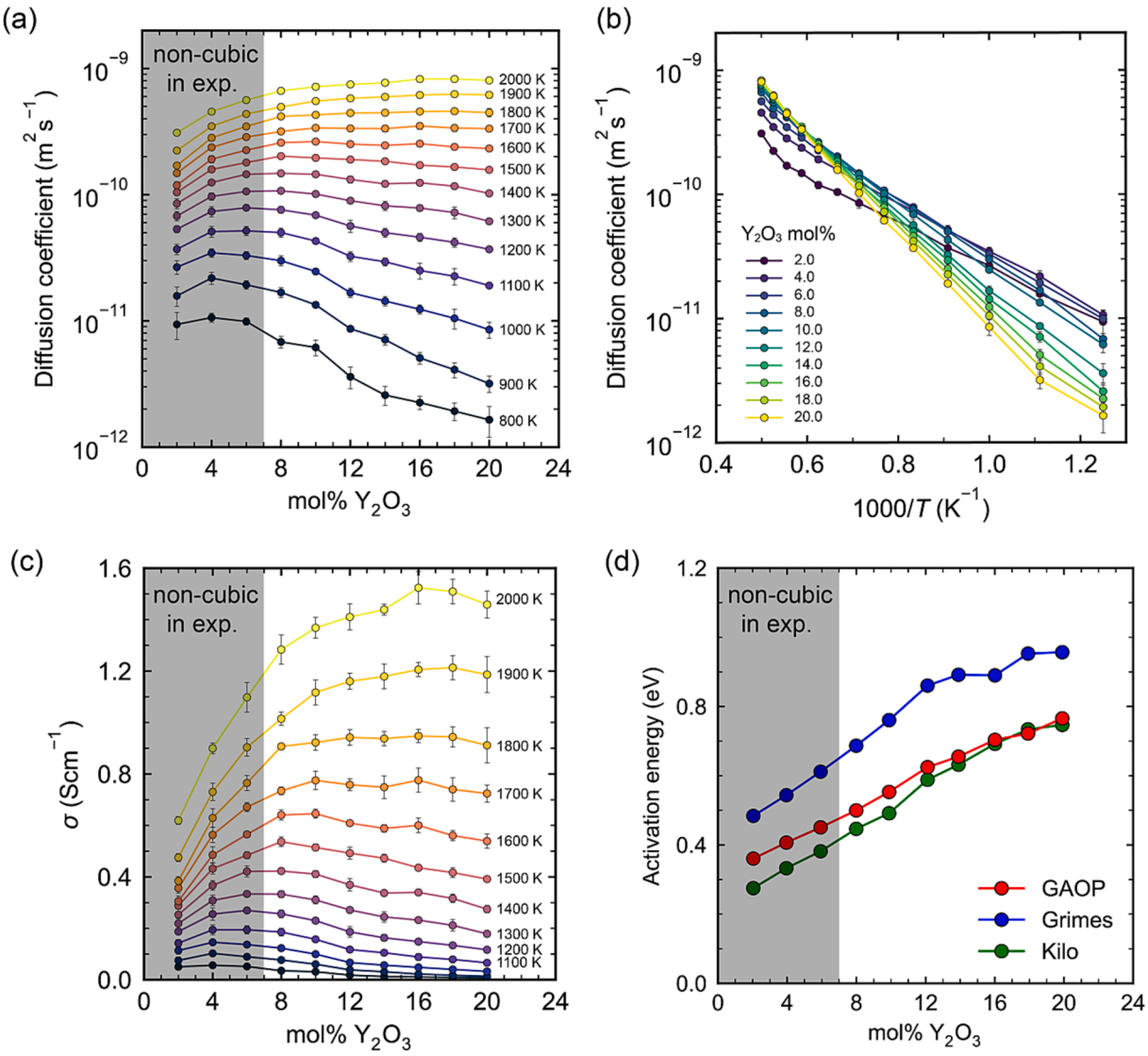

Fig. 7. (a,b) Diffusion coefficients of oxide ions as a function of (a) Y_2O_3 concentration and (b) temperature. (c) Conductivities as a function of Y_2O_3 concentration. (d) Activation energies as a function of Y_2O_3 concentration. The GAOP was used for the calculation. The results using the potentials reported by Grimes et al. [26] and by Kilo et al. [13] were also shown in d. Note that in the experiment, the cubic phase is fully stabilized at Y_2O_3 concentrations above 8 mol%. In the calculation, the cubic phase is stable even at the Y_2O_3 concentrations lower than 8 mol% (gray region in a, c, and d), and the diffusion coefficient and conductivity are overestimated in the region.

$$Z_s = \frac{\sum_j^M \sum_k^6 \left(S_{jk}^{\mathrm{DFT}} - S_{jk}^{\mathrm{EIP}}\right)^2}{6M \sum_j^M \sum_k^6 \left(S_{jk}^{\mathrm{DFT}}\right)^2}, \tag{7}$$

where M is the number of configurations for fitting, N_j is the number of atoms contained in the jth configuration. E_j^{DFT} and E_j^{EIP} are the DFT and EIP energies. Note that these energies are referenced to the energies of the fully relaxed configuration (cubic ZrO_2 model and 10YSZ model with the lowest energy). $\boldsymbol{F}_{ij}^{\mathrm{DFT}}$ and $\boldsymbol{F}_{ij}^{\mathrm{EIP}}$ are the DFT and EIP force vectors of the ith atom in the jth configuration, and S_{jk}^{DFT} and S_{jk}^{EIP} are the DFT and EIP stress tensor components of the jth configuration. The values of w_e, w_f, and w_s were set to 50,000, 30,000, and 20,000, respectively. Note that we also tested the optimization with another set of weight parameters ($w_e = 30{,}000$, $w_f = 50{,}000$, and $w_s = 20{,}000$) and found that the accuracy of the obtained potentials did not change significantly. The energies, forces, and stresses of EIPs were calculated using the Large-scale Atomic/Molecular Massively Parallel Simulator (LAMMPS) [48].

2.3. Material properties

Elastic constants of cubic ZrO_2 were calculated using the General Utility Lattice Program (GULP) [49] for the EIPs. For *ab initio* calculations, we calculated the elastic constants using in-house python scripts utilizing the *elastic* module implemented in pymatgen code [50], with norm strains from −2.0 to 2.0 % in 0.2 % increments and shear strains from −12 % to 12 % in 1 % increments.

Phonon band structures of cubic ZrO_2 were calculated using the finite displacement method implemented in Phonopy [51,52]. An atomic displacement distance of 0.01 Å was employed to derive the second-order force constants. 2 × 2 × 2 supercells with the cell size larger than 10 Å were used in these calculations to avoid the self-interactions between displaced atoms.

MD calculations were performed using the LAMMPS code. To estimate the melting point and coefficient of thermal expansion (CTE) of cubic ZrO_2 and 10YSZ, we created 6 × 6 × 6 supercells of ZrO_2 and 10YSZ with the cell length of approximately 30 Å. To reach thermal equilibrium and promote oxide-ion diffusion, an MD simulation using

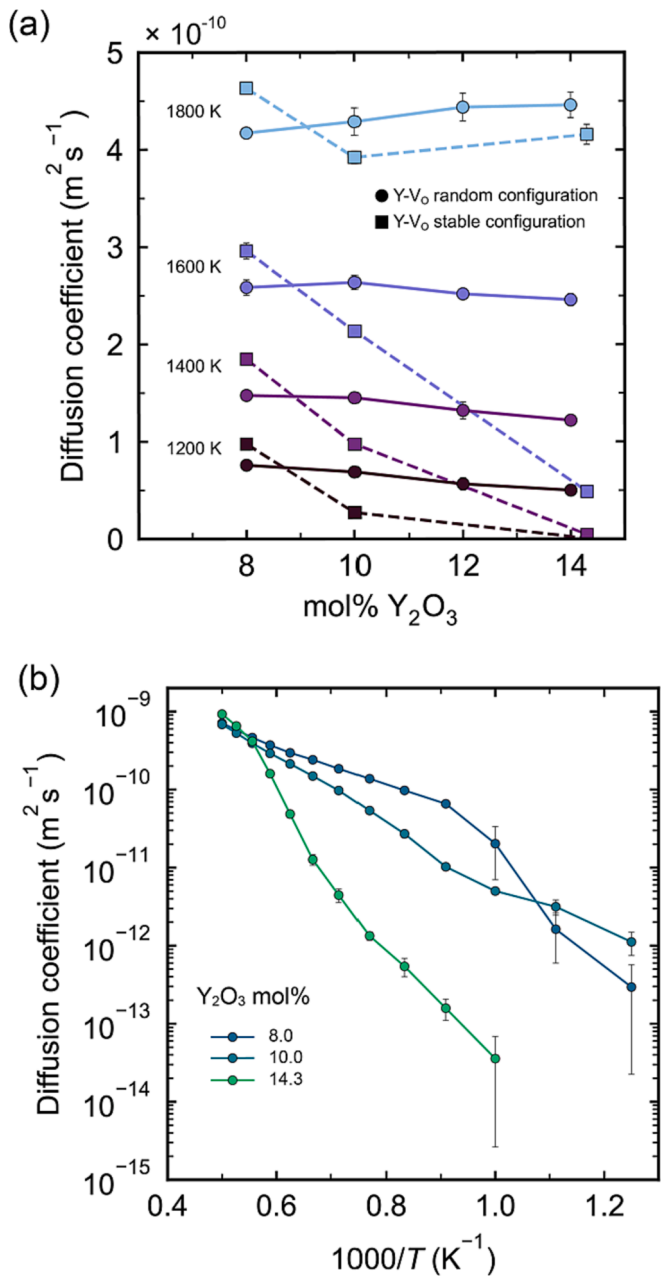

Fig. 8. (a) Comparison of diffusion coefficients obtained with random and stable defect configurations. (b) Diffusion coefficients obtained with stable defect configurations at 0 K as a function of temperature. The stable configurations used were those reported by Guan et al. [30] The GAOP was used for the calculation.

the supercell was performed for 1 ns with a timestep of 1 fs, using temperature scaling at 2000 K, followed by a 2-ns MD simulation to decrease the temperature from 2000 K to 1 K. Then, the calculation for the melting points and CTEs were carried out for 50 ns (50,000,000 steps), slowly increasing the temperature from 1 to 5000 K.

Diffusion coefficients D of oxide ions were also calculated using the LAMMPS code. To obtain statistically accurate diffusion coefficients, we created five $5 \times 5 \times 5$ supercells with random distributions of Y and V_O at 10 different Y_2O_3 concentrations ranging from 0.02 to 0.20 mol%. For each model, the diffusion coefficients were calculated at 13 different temperatures ranging from 800 to 2000 K. We also calculated the diffusion coefficients of 8YSZ, 10YSZ and 14.3YSZ models with the stable defect configurations at 0 K reported by Guan *et al* [30]. For these models, five calculations with different initial atomic velocities were performed on the supercells expanded to contain approximately 2000 atoms. Total number of calculations was 845. The calculation started with a MD simulation with NPT ensemble for 0.1 ns to determine the equilibrium cell length at the target temperature. With the cell length fixed (NVT ensemble), a MD simulation was performed for 0.4 ns to ensure thermal equilibrium states. Then, mean squared displacement (MSD) of oxide ions, $\langle \Delta r(t)^2 \rangle$, was calculated for 1 ns. The self-diffusion coefficients of oxide ions were estimated according to the following equation:

$$D = \lim_{t \to \infty} \frac{\langle \Delta r(t)^2 \rangle}{6t}, \tag{8}$$

where t is the simulation time. Finally, the average diffusion coefficient of the five models were obtained for each Y_2O_3 concentration and each MD temperature. The activation energies of oxide-ion diffusion were calculated from Arrhenius plots in the temperature range from 1100 to 1700 K.

The association energies between Y'_{Zr}-$V^{\bullet\bullet}_O$ and Y'_{Zr}-Y'_{Zr} pairs were calculated using the GULP code. A 5x5x5 supercell of cubic ZrO_2 was prepared. For all possible non-equivalent configurations of two defects in the supercell, the energies were obtained by optimizing the atomic positions with the cell volume fixed (association models). The energy difference between the target model and the model with the farthest defect distance (about 20 Å) is defined as the association energy.

3. Results and discussion

3.1. Developed potential

Fig. 2 shows three and one examples of Z value convergence with respect to generations for the first and second genetic algorithm fitting, respectively. The Z values converged rapidly against generations, especially in the second fitting, due to the small number of fitting parameters. Although the mutation rate was set as high as 40 %, the final Z values shows a wide range from 1.12 to 5.60 in the first fitting, depending on the initial population with random potential parameters. This means that the potential parameters readily fall into local minima. The optimal potential parameters determined by the genetic algorithm are listed in Table 1.

To evaluate the performance of the developed GAOP, root mean squared errors (RMSEs) of energy, force, and stress were calculated for the training and test datasets, as shown in Fig. 3a. The points are aligned on the diagonal line without any deviated points, indicating the good reproducibility of DFT energy, force, and stress by the GAOP. The RMSEs for the training and test datasets are as low as 9.2 and 10.6 meV/atom for energy, 544 and 543 meV/Å for force, and 0.147 and 0.149 GPa for stress, respectively. Similar errors for the training and test datasets indicate that the Buckingham potential parameters were properly optimized without overfitting due to its simple and physics-based equations and the large number of training data.

For comparison, the errors of the Buckingham potentials reported by Grimes *et al.* [26] and Kilo *et al.* [13] were also calculated and shown in Fig. 3b and 3c. The energies, forces, and stresses of these potentials are linearly correlated with the *ab initio* results, reproducing the qualitative trends. However, these potentials overestimate the magnitudes of energy, force, and stress, and the points in Fig. 3b and 3c are distributed over a wide range than the GAOP. Consequently, the RMSEs are significantly higher than the GAOP as seen in Fig. 3 (The errors of GAOP are less than 8 % for energy, 27 % for force, 35 % for stress, compared to the potentials by Grimes and Kilo). We note that it is not possible to judge the superiority or inferiority of these potentials from this result because of the different fitting targets used in their creation. Yet, it can be said that the GAOP perform better than the previously reported EIPs in terms of the reproducibility of *ab initio* calculations.

3.2. Structure and mechanical properties

From here, we discuss various properties estimated using the GAOP in comparison with the experimental and computational results reported previously. The calculated lattice constant a of c-ZrO_2 was 5.067 Å for the *ab initio* calculation and 5.075 Å for the GAOP, with a small error of 0.16 %. The error in the average supercell length of 10YSZ models is also small at −0.28 %, with a being 10.275 Å for the *ab initio* calculation and 10.246 Å for the GAOP. Although Y_2O_3 was not included in the training dataset, the lattice constant of Y_2O_3 was calculated to be 10.543 Å by the GAOP, in good agreement with the value of 10.540 Å calculated by the *ab initio* calculation. These results means that the GAOP is capable of reproducing the cell size of ZrO_2-Y_2O_3 system sufficiently. The elastic constants C_{11}, C_{12}, and C_{44} for cubic ZrO_2 were calculated to be 556.8, 103.9, and 64.7 GPa by the *ab initio* calculation, and 399.9, 70.8, and 69.7 GPa by the GAOP, respectively. Although C_{11} and C_{12} is underestimated in the GAOP, the trend in elastic constants is qualitatively reproduced. These calculated values are also similar to the experimentally determined elastic constants for YSZ with 11.1 mol% Y_2O_3 at 293 K [53], namely 403.5 GPa for C_{11}, 102.4 GPa for C_{12}, and 59.9 GPa for C_{44}. Note that C_{11}, C_{12}, and C_{44} are overestimated with other Buckingham potentials, with the values of 709.2, 134.1, and 129.4 GPa for the Grimes potential and 596.2, 118.6, and 104.0 GPa for the Kilo potential.

3.3. Thermal properties

Fig. 4 shows the phonon band structures determined by *ab initio* calculations, the GAOP, and the potential reported by Grimes *et al.* The frequency range of phonons are overestimated by the Grimes potential, whereas in the GAOP they are in good agreement with the *ab initio* results. This is due to the improved reproducibility of interatomic forces, as can be seen in Fig. 3. The *ab initio* calculations show phonons with imaginary frequencies, which represent the phase transition from cubic to more energetically stable tetragonal phase in pure ZrO_2 [54,55]. The GAOP shows phonon dispersions without any imaginary modes, which is caused by our fitting procedure considering only cubic ZrO_2 and 10YSZ. While the absence of imaginary modes is a disadvantage of the GAOP in terms of reproducibility of ZrO_2 polymorphs, it can be regarded as a technical merit when the effect of phase transitions needs to be excluded to simplify the analysis, *e.g.*, behavior of Y segregation nearby cubic ZrO_2 grain boundaries at 0 K.

The melting points and coefficients of thermal expansion (CTEs) of cubic ZrO_2 and 10YSZ were determined using the GAOP and MD simulations. The volumes of the cells as a function of temperature are shown in Fig. 5. The calculated melting points are about 3060 K for cubic ZrO_2 and 3020 K for 10YSZ, which are consistent with the measured melting point of about 2970 and 3040 K for pure ZrO_2 and 10YSZ, respectively [7]. The linear CTEs calculated from the temperature between 300 and 600 K are 15.4×10^{-6} K^{-1} for ZrO_2 and 8.6×10^{-6} K^{-1} for 10 YSZ. The calculated CTE for 10YSZ agrees with the measured value of 8.9×10^{-6} K^{-1} [56]. This agreement results from the improved reproducibility of stresses, as shown in Fig. 3.

3.4. Oxide-ion conduction

Before investigating oxide-ion conduction in the YSZ models, the association energies of Y'_{Zr}-$V_O^{\bullet\bullet}$ and Y'_{Zr}-Y'_{Zr} pairs were calculated by varying their distances as shown in Fig. 6. The pair of Y'_{Zr} and $V_O^{\bullet\bullet}$ exhibit negative activation energies, indicating that these defects are attractive to each other. The association is strongest at the second nearest neighbor position. On the other hand, the Y'_{Zr}-Y'_{Zr} pair exhibits positive association energies, indicating that the defects are repulsive to each other. These results are in agreement with the association energies calculated by *ab initio* calculations [19].

Fig. 7a and b show the calculated diffusion coefficients D of oxide ions in YSZ as a function of Y_2O_3 concentration and temperature, respectively. The defects Y and V_O were randomly introduced in the YSZ models. At Y_2O_3 concentrations where cubic structure is experimentally stable (≥8 mol%), 8YSZ exhibit highest diffusion coefficients over a wide temperature (from 800 to 1500 K), consistent with experimental and computational results [12,14,18]. The order of the diffusion coefficient of 8YSZ and 10YSZ ranges from 10^{-11} to 10^{-10} m^2s^{-1} above 1000 K, also agreeing with many experiments and computations [11,13,14,16,18,20,57,58]. It is reported that oxide-ion diffusion is significantly decreased at low Y_2O_3 concentration around 4 mol% and high temperature at 1273 K [59], because of the formation of lower-symmetry tetragonal structure. This trend was not observed in Fig. 7a, due to the hypothetical cubic phase stability of the GAOP.

Fig. 7c shows the conductivities σ estimated from the diffusion coefficients and the following Nernst-Einstein relation:

$$\sigma = \frac{q^2 DN}{VN_A}\left(\frac{F^2}{RT}\right), \tag{9}$$

where q is the charge of the mobile ion (oxide ion), N is the number of oxide ions in the cell, V is the volume of the cell, N_A is the Avogadro constant, F is the Faraday constant, R is the gas constant, and T is the temperature. The calculated σ for 8YSZ are 0.19, 0.33, and 0.64 Sm^{-1} at 1100, 1300 and 1600 K, respectively. On the other hand, one of the experiments showed that σ for 8YSZ are 0.06, 0.19, 0.52 Scm^{-1} at 1073, 1273, and 1573 K [12]. The calculated value at 1600 K is close to the experimental value, but the temperature dependence is less significant in the GAOP calculations. This is caused by the underestimation of activation energy of oxide-ion diffusion, as shown in Fig. 7d. Although the increasing trend of activation energy as a function of Y_2O_3 concentration is consistent with experiments, the magnitude is lower than that of experiments ranging from 0.6 to 1.4 eV [12,14,15]. Possible reasons for this are the assumption of random Y and V_O configurations in our calculations, and the correlated motion of oxygen due to high defect concentrations. Quantitative comparisons of diffusion coefficients and conductivities between calculations and experiments require the determination of defect configurations using Monte Carlo simulations and the calculation of the Haven ratio (See Discussion S1 and Fig. S3 for the Haven ratio of 8YSZ). Under the same computational conditions but using the Grimes potential, the calculated σ for 8YSZ are 0.02, 0.07, and 0.16 Sm^{-1} at 1100, 1300 and 1600 K, respectively, lower than the measured values of ref. [12] (Fig. S4). The activation energies are about 0.2 eV higher than those of the GAOP (Fig. 7d). Using the Kilo potential, the calculated σ for 8YSZ are 0.16, 0.26, and 0.45 Sm^{-1} at 1100, 1300 and 1600 K, respectively (Fig. S5). The activation energies are similar or about 0.1 eV less than those of the GAOP (Fig. 7d). These two potentials showed the maximum conductivity in 8YSZ from 800 to 2000 K.

Kondoh *et al.* demonstrated that thermal aging on YSZ samples, which should affect the distribution of Y and V_O, significantly changes oxide-ion conductivity [12]. Furthermore, Guan *et al.* obtained stable configurations of Y and V_O at 0 K in YSZ using MLPs [30], and claimed that the consideration of these stable configurations can explain the dependence of conductivity on Y_2O_3 concentration and temperature observed in experiments [31]. To examine whether the GAOP can reproduce the effect of defect configurations on oxide-ion conduction, the diffusion coefficients in the stable configurations reported by Guan were also calculated, as shown in Fig. 8. With the stable defect configurations, diffusion coefficients drop at high Y_2O_3 concentration of 14.3 mol% at lower temperatures as seen in Fig. 8. This is consistent with the low conductivity of YSZ with high Y_2O_3 concentration in experiments [14]. In addition, the conductivity shows different trends at low and high temperature ranges in 8YSZ, which also agreeing with the MLP calculations. These results are presumably because oxide-ion vacancies are strongly trapped by Y at low temperatures in the stable defect configurations (as mentioned in former part of this section), but thermal energy at higher temperatures causes the vacancies to be released from

the trap and conductivity increases. The activation energy of high temperature region is 0.46 eV for GAOP, which is not significantly different from 0.63 eV obtained using an MLP. These consistencies demonstrate that the GAOP reproduces the ionic conduction at least qualitatively, including the interactions between defect complexes. Since the stable configurations of Guan et al. were created using models with relatively small number of atoms (46–79 atoms), the relationship between defect configurations and oxide-ion conductivity may be more statistically determined if stable configurations in larger cells are obtained using the GAOP and Monte Carlo methods, for example.

4. Conclusions

We optimized the EIPs for cubic ZrO_2 and 10YSZ using the genetic algorithm and *ab initio* calculations. The developed GAOP reproduced the energy, force acting on atoms, and stress of the *ab initio* calculations more accurately than previously reported EIPs. As a result, the structural, mechanical, thermal, and ionic conduction properties calculated by the GAOP showed at least qualitative agreements with the *ab initio* results and/or experiments, and in many cases the values were close. Using the GAOP, large-scale MD calculations for a wide variety of defect configurations as well as identification of Y segregated grain boundary structures can be performed with higher accuracy than previous EIPs. The combination with MLP-based and *ab initio* calculations will enable more statistical and accurate characterization of YSZ.

CRediT authorship contribution statement

Susumu Fujii: Conceptualization, Methodology, Software, Validation, Formal analysis, Investigation, Resources, Writing – original draft, Visualization, Project administration, Funding acquisition. **Akihide Kuwabara:** Resources, Writing – review & editing, Project administration, Funding acquisition.

Declaration of competing interest

The authors declare that they have no known competing financial interests or personal relationships that could have appeared to influence the work reported in this paper.

Data availability

Data will be made available on request.

Acknowledgements

A part of this study was supported by Next Generation Zirconia Social Cooperation Program, The University of Tokyo. SF was supported by a Grant-in-Aid for Early-Career Scientists (Grant Numbers JP20K15034 and JP23K13544) and Grants-in-Aid for Scientific Research on Innovative Areas (Grant Numbers JP20H05195 and JP19H05786) from the Japan Society for the Promotion of Science (JSPS).

Appendix A. Supplementary material

Supplementary data to this article can be found online at https://doi.org/10.1016/j.commatsci.2023.112722.

References

[1] B.C.H. Steele, A. Heinzel, Materials for fuel-cell technologies, Nature. 414 (2001) 345–352, https://doi.org/10.1038/35104620.
[2] B. Shri Prakash, S. Senthil Kumar, S.T. Aruna, Properties and development of Ni/YSZ as an anode material in solid oxide fuel cell: A review, Renew. Sustain. Energy Rev. 36 (2014) 149–179, https://doi.org/10.1016/j.rser.2014.04.043.
[3] N.P. Padture, Thermal Barrier Coatings for Gas-Turbine Engine Applications, Science. 296 (2002) 280–284, https://doi.org/10.1126/science.1068609.
[4] R.H.J. Hannink, P.M. Kelly, B.C. Muddle, Transformation toughening in zirconia-containing ceramics, J. Am. Ceram. Soc. 83 (2000) 461–487, https://doi.org/10.1111/j.1151-2916.2000.tb01221.x.
[5] K. Matsui, H. Yoshida, Y. Ikuhara, Review: microstructure-development mechanism during sintering in polycrystalline zirconia, Int. Mater. Rev. 63 (2018) 375–406, https://doi.org/10.1080/09506608.2017.1402424.
[6] J. Chevalier, A. Liens, H. Reveron, F. Zhang, P. Reynaud, T. Douillard, L. Preiss, V. Sergo, V. Lughi, M. Swain, N. Courtois, Forty years after the promise of «ceramic steel?»: Zirconia-based composites with a metal-like mechanical behavior, J. Am. Ceram. Soc. 103 (2020) 1482–1513, https://doi.org/10.1111/jace.16903.
[7] O.R.J. Ackermann, S.P. Garg, E.G. Rauh, High-Temperature Phase Diagram for the System Zr-O, J. Am. Ceram. Soc. 60 (1977) 341–345, https://doi.org/10.1111/j.1151-2916.1977.tb15557.x.
[8] M. Jayaratna, M. Yoshimura, S. Somiya, Subsolidus Phase Relations in the Pseudoternary System ZrO_2-$YO_{1.5}$-$CrO_{1.5}$ in Air, J. Am. Ceram. Soc. 67 (1984) c240–c242, https://doi.org/10.1111/j.1151-2916.1984.tb19496.x.
[9] P. Li, I.-W. Chen, J.E. Penner-Hahn, Effect of Dopants on Zirconia Stabilization—An X-ray Absorption Study: I, Trivalent Dopants, J. Am. Ceram. Soc. 77 (1994) 118–128, https://doi.org/10.1111/j.1151-2916.1994.tb06964.x.
[10] P. Li, I.-W. Chen, J.E. Penner-Hahn, Effect of Dopants on Zirconia Stabilization—An X-ray Absorption Study: II, Tetravalent Dopants, J. Am. Ceram. Soc. 77 (1994) 1281–1288, https://doi.org/10.1111/j.1151-2916.1994.tb05403.x.
[11] P.S. Manning, J.D. Sirman, R.A. De Souza, J.A. Kilner, The kinetics of oxygen transport in 9.5 mol % single crystal yttria stabilised zirconia, Solid State Ionics. 100 (1997) 1–10, https://doi.org/10.1016/s0167-2738(97)00345-7.
[12] J. Kondoh, T. Kawashima, S. Kikuchi, Y. Tomii, Y. Ito, Effect of Aging on Yttria-Stabilized Zirconia: I. A Study of Its Electrochemical Properties, J. Electrochem. Soc. 145 (1998) 1527–1536, https://doi.org/10.1149/1.1838515.
[13] M. Kilo, C. Argirusis, G. Borchardt, R.A. Jackson, Oxygen diffusion in yttria stabilised zirconia - Experimental results and molecular dynamics calculations, Phys. Chem. Chem. Phys. 5 (2003) 2219–2224, https://doi.org/10.1039/b300151m.
[14] M. Weller, R. Herzog, M. Kilo, G. Borchardt, S. Weber, S. Scherrer, Oxygen mobility in yttria-doped zirconia studied by internal friction, electrical conductivity and tracer diffusion experiments, Solid State Ionics. 175 (2004) 409–413, https://doi.org/10.1016/j.ssi.2003.12.044.
[15] C. Ahamer, A.K. Opitz, G.M. Rupp, J. Fleig, Revisiting the Temperature Dependent Ionic Conductivity of Yttria Stabilized Zirconia (YSZ), J. Electrochem. Soc. 164 (2017) F790–F803, https://doi.org/10.1149/2.0641707jes.
[16] M.S. Khan, M.S. Islam, D.R. Bates, Cation doping and oxygen diffusion in zirconia: A combined atomistic simulation and molecular dynamics study, J. Mater. Chem. 8 (1998) 2299–2307, https://doi.org/10.1039/a803917h.
[17] P.K. Schelling, S.R. Phillpot, D. Wolf, Mechanism of the Cubic-to-Tetragonal Phase Transition in Zirconia and Yttria-Stabilized Zirconia by Molecular-Dynamics Simulation, J. Am. Ceram. Soc. 84 (2001) 1609–1619, https://doi.org/10.1111/j.1151-2916.2001.tb00885.x.
[18] R. Krishnamurthy, Y.G. Yoon, D.J. Srolovitz, R. Car, Oxygen diffusion in yttria-stabilized zirconia: A new simulation model, J. Am. Ceram. Soc. 87 (2004) 1821–1830, https://doi.org/10.1111/j.1151-2916.2004.tb06325.x.
[19] R. Pornprasertsuk, P. Ramanarayanan, C.B. Musgrave, F.B. Prinz, Predicting ionic conductivity of solid oxide fuel cell electrolyte from first principles, J. Appl. Phys. 98 (2005), 103513, https://doi.org/10.1063/1.2135889.
[20] V.V. Sizov, M.J. Lampinen, A. Laaksonen, Molecular dynamics simulation of oxygen diffusion in cubic yttria-stabilized zirconia: Effects of temperature and composition, Solid State Ionics. 266 (2014) 29–35, https://doi.org/10.1016/j.ssi.2014.08.003.
[21] T. Oyama, M. Yoshiya, H. Matsubara, K. Matsunaga, Numerical analysis of solute segregation at Σ5 (310)/[001] symmetric tilt grain boundaries in Y_2O_3-doped ZrO_2, Phys. Rev. B - Condens. Matter Mater. Phys. 71 (2005), 224105, https://doi.org/10.1103/PhysRevB.71.224105.
[22] T. Yokoi, M. Yoshiya, H. Yasuda, Nonrandom point defect configurations and driving force transitions for grain boundary segregation in trivalent cation doped ZrO_2, Langmuir. 30 (2014) 14179–14188, https://doi.org/10.1021/la503338x.
[23] B. Feng, T. Yokoi, A. Kumamoto, M. Yoshiya, Y. Ikuhara, N. Shibata, Atomically ordered solute segregation behaviour in an oxide grain boundary, Nat. Commun. 7 (2016) 11079, https://doi.org/10.1038/ncomms11079.
[24] M. Jaipal, A. Chatterjee, Relative Occurrence of Oxygen-Vacancy Pairs in Yttrium-Containing Environments of Y_2O_3-Doped ZrO_2 Can Be Crucial to Ionic Conductivity, J. Phys. Chem. C. 121 (2017) 14534–14543, https://doi.org/10.1021/acs.jpcc.7b05329.
[25] M. Jaipal, A. Chatterjee, Effect of the Σ5(310)/[001] tilt grain boundary on oxygen-ion movement in yttria-stabilized zirconia: Insights from molecular dynamics, Acta Mater. 165 (2019) 307–314, https://doi.org/10.1016/j.actamat.2018.11.064.
[26] L. Minervini, R.W. Grimes, K.E. Sickafus, Disorder in pyrochlore oxides, J. Am. Ceram. Soc. 83 (2000) 1873–1878, https://doi.org/10.1111/j.1151-2916.2000.tb01484.x.
[27] J.C. Madrid Madrid, J. Matsuda, K. Leonard, H. Matsumoto, K.K. Ghuman, Molecular dynamics study of oxygen-ion diffusion in yttria-stabilized zirconia grain boundaries, J. Mater. Chem. A. 10 (2022) 2567–2579, https://doi.org/10.1039/d1ta08309k.
[28] S. Madhual, K. Pramanik, P.P. Kumar, Understanding oxide ion transport in yttria stabilized zirconia: fresh insights from molecular dynamics simulations, Phys. Chem. Chem. Phys. 24 (2022) 18281–18290, https://doi.org/10.1039/d2cp01377k.

[29] C. Wang, A. Tharval, J.R. Kitchin, A density functional theory parameterised neural network model of zirconia, Mol. Simul. 44 (2018) 623–630, https://doi.org/10.1080/08927022.2017.1420185.
[30] S.H. Guan, K.X. Zhang, C. Shang, Z.P. Liu, Stability and anion diffusion kinetics of Yttria-stabilized zirconia resolved from machine learning global potential energy surface exploration, J. Chem. Phys. 152 (2020), 094703, https://doi.org/10.1063/1.5142591.
[31] S.H. Guan, C. Shang, Z.P. Liu, Resolving the Temperature and Composition Dependence of Ion Conductivity for Yttria-Stabilized Zirconia from Machine Learning Simulation, J. Phys. Chem. C. 124 (2020) 15085–15093, https://doi.org/10.1021/acs.jpcc.0c04331.
[32] C. Verdi, F. Karsai, P. Liu, R. Jinnouchi, G. Kresse, Thermal transport and phase transitions of zirconia by on-the-fly machine-learned interatomic potentials, Npj Comput. Mater. 7 (2021) 156, https://doi.org/10.1038/s41524-021-00630-5.
[33] R. Ganser, S. Bongarz, A. Von Mach, L. Azevedo Antunes, A. Kersch, Piezo- and Pyroelectricity in Zirconia: A Study with Machine-Learned Force Fields, Phys. Rev. Appl. 18 (2022), 054066, https://doi.org/10.1103/PhysRevApplied.18.054066.
[34] P. Liu, C. Verdi, F. Karsai, G. Kresse, Phase transitions of zirconia: Machine-learned force fields beyond density functional theory, Phys. Rev. B. 105 (2022) L060102, https://doi.org/10.1103/PhysRevB.105.L060102.
[35] A. Seko, Machine learning potentials for multicomponent systems: The Ti-Al binary system, Phys. Rev. B. 102 (2020), 174104, https://doi.org/10.1103/PhysRevB.102.174104.
[36] S. Fujii, A. Seko, Structure and lattice thermal conductivity of grain boundaries in silicon by using machine learning potential and molecular dynamics, Comput. Mater. Sci. 204 (2022), 111137, https://doi.org/10.1016/j.commatsci.2021.111137.
[37] A. Rohskopf, H.R. Seyf, K. Gordiz, T. Tadano, A. Henry, Empirical interatomic potentials optimized for phonon properties, Npj Comput. Mater. 3 (2017) 27, https://doi.org/10.1038/s41524-017-0026-y.
[38] X. Chen, L.F. Wang, X.Y. Gao, Y.F. Zhao, D.Y. Lin, W.D. Chu, H.F. Song, Machine learning enhanced empirical potentials for metals and alloys, Comput. Phys. Commun. 269 (2021), 108132, https://doi.org/10.1016/j.cpc.2021.108132.
[39] Z. Fan, Y. Wang, X. Gu, P. Qian, Y. Su, T. Ala-Nissila, A minimal Tersoff potential for diamond silicon with improved descriptions of elastic and phonon transport properties, J. Phys. Condens. Matter. 32 (2020), https://doi.org/10.1088/1361-648X/ab5c5f.
[40] S. Fujii, K. Shimazaki, A. Kuwabara, Empirical interatomic potentials for ZrO_2 and YSZ polymorphs : Application to a tetragonal ZrO_2 grain boundary, Acta Mater. 262 (2024), 119460, https://doi.org/10.1016/j.actamat.2023.119460.
[41] A. Seko, A. Togo, I. Tanaka, Group-theoretical high-order rotational invariants for structural representations: Application to linearized machine learning interatomic potential, Phys. Rev. B. 99 (2019), 214108, https://doi.org/10.1103/PhysRevB.99.214108.
[42] P.E. Blöchl, Projector augmented-wave method, Phys. Rev. B. 50 (1994) 17953–17979, https://doi.org/10.1103/PhysRevB.50.17953.
[43] G. Kresse, J. Hafner, Ab initio molecular-dynamics simulation of the liquid-metal–amorphous-semiconductor transition in germanium, Phys. Rev. B. 49 (1994) 14251–14269, https://doi.org/10.1103/PhysRevB.49.14251.
[44] G. Kresse, J. Furthmüller, Efficient iterative schemes for ab initio total-energy calculations using a plane-wave basis set, Phys. Rev. B. 54 (1996) 11169–11186, https://doi.org/10.1103/PhysRevB.54.11169.
[45] J.P. Perdew, A. Ruzsinszky, G.I. Csonka, O.A. Vydrov, G.E. Scuseria, L. A. Constantin, X. Zhou, K. Burke, Restoring the density-gradient expansion for exchange in solids and surfaces, Phys. Rev. Lett. 100 (2008), 136406, https://doi.org/10.1103/PhysRevLett.100.136406.
[46] H.J. Monkhorst, J.D. Pack, Special points for Brillouin-zone integrations, Phys. Rev. B. 13 (1976) 5188–5192, https://doi.org/10.1103/PhysRevB.13.5188.
[47] G.V. Lewis, C.R.A. Catlow, Potential models for ionic oxides, J. Phys. C Solid State Phys. 18 (1985) 1149–1161, https://doi.org/10.1088/0022-3719/18/6/010.
[48] S. Plimpton, Fast Parallel Algorithms for Short-range molecular dynamics, J. Comput. Phys. 117 (1995) 1–19, https://doi.org/10.1006/jcph.1995.1039.
[49] J.D. Gale, GULP: A computer program for the symmetry-adapted simulation of solids, J. Chem. Soc. Faraday Trans. 93 (1997) 629–637, https://doi.org/10.1039/a606455h.
[50] S.P. Ong, W.D. Richards, A. Jain, G. Hautier, M. Kocher, S. Cholia, D. Gunter, V. L. Chevrier, K.A. Persson, G. Ceder, Python Materials Genomics (pymatgen): A robust, open-source python library for materials analysis, Comput. Mater. Sci. 68 (2013) 314–319, https://doi.org/10.1016/j.commatsci.2012.10.028.
[51] A. Togo, I. Tanaka, First principles phonon calculations in materials science, Scr. Mater. 108 (2015) 1–5, https://doi.org/10.1016/j.scriptamat.2015.07.021.
[52] A. Togo, First-principles Phonon Calculations with Phonopy and Phono3py, J. Phys. Soc. Japan. 92 (2023), 012001, https://doi.org/10.7566/JPSJ.92.012001.
[53] H.M. Kandil, J.D. Greiner, J.F. Smith, Single-Crystal Elastic Constants of Yttria-Stabilized Zirconia in the Range 20° to 700°C, J. Am. Ceram. Soc. 67 (1984) 341–346, https://doi.org/10.1111/j.1151-2916.1984.tb19534.x.
[54] K. Parlinski, Z. Li, Y. Kawazoe, First-principles determination of the soft mode in cubic ZrO_2, Phys. Rev. Lett. 78 (1997) 4063–4066, https://doi.org/10.1103/PhysRevLett.78.4063.
[55] A. Kuwabara, T. Tohei, T. Yamamoto, I. Tanaka, Ab initio lattice dynamics and phase transformations of ZrO_2, Phys. Rev. B - Condens. Matter Mater. Phys. 71 (2005), 064301, https://doi.org/10.1103/PhysRevB.71.064301.
[56] H. Hayashi, T. Saitou, N. Maruyama, H. Inaba, K. Kawamura, M. Mori, Thermal expansion coefficient of yttria stabilized zirconia for various yttria contents, Solid State Ionics. 176 (2005) 613–619, https://doi.org/10.1016/j.ssi.2004.08.021.
[57] T. Arima, K. Fukuyo, K. Idemitsu, Y. Inagaki, Molecular dynamics simulation of yttria-stabilized zirconia between 300 and 2000 K, J. Mol. Liq. 113 (2004) 67–73, https://doi.org/10.1016/j.molliq.2004.02.038.
[58] R. Devanathan, W.J. Weber, S.C. Singhal, J.D. Gale, Computer simulation of defects and oxygen transport in yttria-stabilized zirconia, Solid State Ionics. 177 (2006) 1251–1258, https://doi.org/10.1016/j.ssi.2006.06.030.
[59] S.P.S. Badwal, Zirconia-based solid electrolytes: microstructure, stability and ionic conductivity, Solid State Ionics. 52 (1992) 23–32, https://doi.org/10.1016/0167-2738(92)90088-7.